Measurement of the Scattering Matrix and Extinction Coefficient of the Chaff Corridor

YANCHUN ZUO, **LIXIN GUO**, (Senior Member, IEEE), **WEI LIU**, (Member, IEEE), **AND JIANYANG DING**, (Graduate Student Member, IEEE)

School of Physics and Optoelectronic Engineering, Xidian University, Xi'an 710071, China

Corresponding author: Lixin Guo (lxguo@xidian.edu.cn)

ABSTRACT This article investigates the strategies to measure the scattering matrix and the extinction coefficient of the chaff corridor. A complete error model is adopted to describe the power transmission properties of the indoor measurement system. Based on this model, a polaristic calibration method is employed to correct the measurement errors. After calibration, a scattering matrix measurement method for different types of chaff corridors is addressed. When dealing with the extinction coefficient measurements, Beer-Lambert's law is introduced to describe the power loss of the electromagnetic wave passing through the chaff corridor. According to this law, a method of the extinction coefficient measurement for the chaff corridor is proposed. Finally, simulations and measurements are conducted to verify the methods presented in this article and obtain the electromagnetic scattering properties of various types of chaff corridors. Experimental results show that the scattering matrix and extinction coefficient are not sensitive to the polarization of the incident wave for uniformly distributed chaff corridor. Besides, high attenuation occurs when electromagnetic wave passes through the chaff corridor.

INDEX TERMS Scattering matrix, extinction coefficient, indoor measurement, chaff corridor.

I. INTRODUCTION

The chaff cloud, emerging as a passive jammer, has been widely used in many battle scenarios for its low cost and high jamming performance. Chaff packages burst open and form a chaff cloud immediately when the target is under attack. The released chaff cloud obstructs the radar and leads to a failure in target detection [1]–[3]. Generally, the chaff cloud consists of a large number of small metal-fibers which can reflect the radar signals to produce a strong echo. To ensure that it has an excellent jamming performance, complex geometric modeling and electromagnetic (EM) scattering evaluation processes are derived before it is put into use.

Many EM computational methods have been presented to determine the EM scattering properties of the chaff cloud. Researchers spontaneously start their efforts with the EM scattering evaluation of a single chaff element [4]–[6]. Van Vleck derived a formula to calculate the radar cross section (RCS) of an arbitrary-length element. The total RCS of the chaff cloud has been evaluated by summing all the

RCSs of wires together with probabilities to pursuit a high calculation efficiency [7], [8]. For polaristic EM scattering evaluation of the chaff cloud, many proposals are firstly put forward to theoretically study the polaristic scattering characteristics of the chaff element with the aid of scattering matrix and Stokes matrix theories [9]–[14]. Based on the matrix descriptions of a single chaff element, the superposition method is then adopted to add all the EM polaristic scatterings of the chaff elements with probability and multiplying rotation matrixes. For both the nonparasitic and polaristic scattering evaluation methods of the chaff cloud mentioned above, the EM coupling between chaff elements is always neglected, which makes the scattering results inaccurate and not reasonable for element-dense chaff cloud. Still, these methods provide an efficient way to evaluate the polaristic scattering properties of the chaff cloud.

Chaff corridor, known as a type of the chaff cloud, plays an important role in electronic countermeasure (ECM). The EM scattering estimation of the chaff corridor has been the subject of many published works [15]–[19]. In most of these works, the radar equation is employed to calculate the transmission and reflection properties of the EM wave in the chaff

---

The associate editor coordinating the review of this manuscript and approving it for publication was Jenny Mahoney.

corridor. Researchers, like S. Kownacki *et al.*, used the power attenuation coefficient to measure the power loss of the EM wave within a unit path length in the chaff corridor [20], [21]. With this parameter, Fang *et al.* studied the transmission characteristics of the EM waves passing through the chaff corridor on a rainy day [22]. One can also evaluate the EM scattering properties of the chaff corridor directly using the probability density functions (PDFs) obtained from experiments [6], [23]. These methods provide an efficient way to access the scattering power of the chaff corridor in a relatively short time. But the accuracy of these methods depends upon the value-reliability of the constants involved in the radar equation and the PDFs of the scattering power.

If one wants to accurately access the EM scattering of the chaff corridor, numerical algorithms can be naturally adopted [24], [25], but they cannot deal with the chaff corridor which contains huge numbers of elements. The reason is that the numerical methods cause a considerable computational burden in solving equations. Besides, the numerical methods can only estimate the EM scattering of the static model of the chaff corridor which is just a sample selected from the model population of the chaff corridor. Therefore, if it is desired to obtain the statistical EM scattering properties of the chaff corridor using the numerical methods, large numbers of chaff corridor models need to be generated and numerically processed. This further leads to an additional computational load.

Experimental study of the EM scattering properties of the chaff cloud (corridor) is an irreplaceable way to investigate some complex factors which are not fully considered in the theoretical analysis [26], [27]. The basic principle of the EM scattering measurements is the radar range equation. Based on this principle, Wang *et al.* chosen a proper emitting and receiving time window for efficient dynamic measurement of the chaff corridor [28]. Zeng *et al.* have experimentally determined the parameters in the PDF of the RCS of the chaff cloud in the S and X band [29]. Zou *et al.* have established a chaff measurement system at a frequency of 94.5 GHz [30]. However, studying the scattering properties of the chaff cloud (corridor) using the presented experimental methods is expensive, especially for the outdoor experiments. More importantly, the geometric model of the chaff cloud (corridor) and experimental conditions are quite hard to be controlled using the methods presented in the available literature, which causes difficulties in comparing the simulation results with the experimental ones.

Based on the EM scattering results obtained by various means, several authors have considered the tactical usage of the chaff cloud (corridor). Yang *et al.* have studied the target detection methods under chaff jamming with GPS/INS by taking the azimuthal in-phase mono-pulse ratio of radar seeker as the test statistic [31]. Widdel *et al.* have exploited the chaff cloud as a tool to detect dynamical features of the atmosphere or conduct emergency communication [32]–[34]. Zak *et al.* have discussed using a source to illuminate the chaff cloud to produce a suitable Doppler frequency on the radar

echo to improve the jamming efficiency. Zuo *et al.* also studied the EM scattering properties of the chaff cloud illuminated by a beam [35]. However, the reliability and effectiveness of these applications are all guaranteed by the accurate EM scattering prediction of the chaff cloud (corridor) before they are put into use.

Although much progress is made in the fields of the geometric modeling and the EM scattering evaluation of the chaff corridor, there are still some problems remained that are not fully resolved. To solve these problems, the main contributions of this article are listed in the following.

(i) The modeling of the chaff corridor. A specific element insertion device is designed and used to make the physical model of the chaff corridor for testing. The geometric model of the chaff corridor is firstly generated on computer. Then, the elements insertion process is performed to produce the physical model of the chaff corridor in accordance with the simulation one. This innovation provides a controllable and precise physical model for measurements. It also provides a possibility to compare the EM simulation with measurement results of the chaff corridor reasonably.

(ii) Experimental study of the scattering matrixes and extinction coefficients of the chaff corridor. Most of the published works focus on the EM scattering evaluation of the chaff corridor, especially the RCS, by running simulations. Even so, the polaristic EM scattering and attenuation properties of the chaff corridor are still rarely addressed from both the aspect of the simulations and the experiments. Besides, many complex factors are ignored in simulations. This article conducts experimental research on the EM scattering and attenuation characteristics of the chaff corridor, which also provides a reasonable way to take an insight into the complex EM scattering phenomenon of the chaff corridor.

(iii) An analytical formula derivation of the calibration and measurement processes of the EM polaristic measurements of the chaff corridor. In most previous works, the polaristic calibration formulas are derived based on the matrix method and the Mason equation, which gives no analytical formulas for the process of the calibration and the measurement. This strategy results in computational complexity in applying these methods. This article proposes an analytical derivation to provide clear descriptions and applicable strategies for the polaristic EM scattering measurement process of the chaff corridor.

On the basis of the analysis presented above, this article is organized as follows. Section I introduces the research background of this article and gives relative progress made by other researchers. Following this, the innovations of this article are put forward. Then, the methods for simulation and physical model establishing of the chaff corridor are addressed in Section II. Next, the principals for the EM scattering matrix and extinction coefficient measurements of the chaff corridor are subsequently presented in Section II. Finally, experiments are conducted and some analysis is performed in Section III to give useful conclusions of the polaristic scattering properties of the chaff corridor.
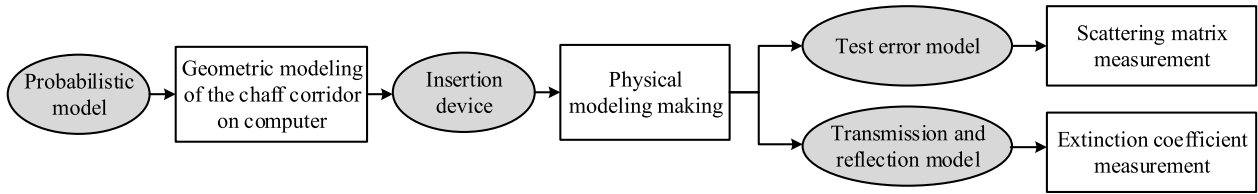
FIGURE 1. The flow chart of the measurement theorem.

II. TEST THEORY FOR EXPERIMENTS

In this section, the methods how to measure the polaristic scattering matrix and the extinction coefficient of the chaff corridor are addressed. The strategies of simulation model generation and the physical model making for the chaff corridor are firstly presented. A specific device is designed for chaff elements insertion to guarantee the fabricating accuracy of the physical model. Then, the test error model is adopted to describe the power transmitting properties of the EM wave in the chamber to perform the calibration process. Next, the theories to obtain the scattering matrix and extinction coefficient of the chaff corridor are proposed, which are applicable for the stepped frequency measurement system. In the end, the test facilities are introduced and the measurement steps are given. The flow chart of the measurement strategies is illustrated in Fig.1.

A. MODELING OF THE CHAFF CLOUD

In this part, the simulation model of the chaff corridor is first established on the computer by programming according to the probabilistic methods. Then, the block-making strategy and a specific insertion device are used to make the physical model of the chaff corridor.

To mathematically describe the model of the chaff corridor, the global coordinates system is first established as Fig.2 (a). In general, the central coordinates' distributions of the chaff elements obey the uniform distribution. Hence if we denote the central coordinates of a chaff element as (x, y, z), then we have

$$\begin{cases} x = x_{\min} + (x_{\max} - x_{\min}) \cdot \text{rand}() \\ y = y_{\min} + (y_{\max} - y_{\min}) \cdot \text{rand}() \\ z = x_{\min} + (z_{\max} - z_{\min}) \cdot \text{rand}() \end{cases} \quad (1)$$

where, $x \in [x_{\min}, x_{\max}], y \in [y_{\min}, y_{\max}], z \in [z_{\min}, z_{\max}]$. $x_{\min}, x_{\max}, y_{\min}, y_{\max}, z_{\min},$ and $z_{\max}$ are the lower and upper bound of the central coordinates of the chaff elements, respectively. The function rand() generates a uniformly distributed random number in the interval $(0, 1)$. Then, the model of the chaff corridor can be obtained by repeating the calculation process for all the chaff elements as (1).

After determining the central coordinates of the chaff elements, now we deal with the orientation selection for each chaff element. The local coordinates system is defined as Fig.2 (b). The origin, designated $(0, 0)$, is located at the geometric center of the chaff element. Besides, the x-axis, y-axis, and z-axis are parallel to that of the global coordinates
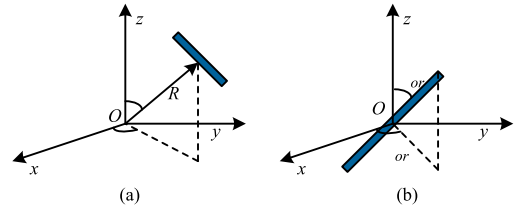

FIGURE 2. The figure of a chaff element in its coordinates system. (a) The coordinates system of the chaff cloud. (b) The coordinates system of the chaff element.
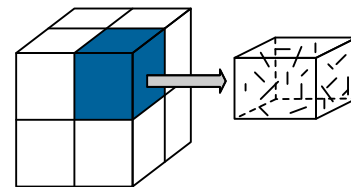

FIGURE 3. The figure of how to make a test model.

system defined in Fig.2 (a). The orientation of a chaff element is specified by the $(\theta_{or}, \varphi_{or})$, θ_{or} is the angle of rotation from the initial meridian plane, and φ_{or} is the angle from the polar axis. When the chaff element is mass uniform and released in thin air, the PDFs of the angle θ_{or} and φ_{or} can be written as

$$f(\theta_{or}) = 1, \quad f(\varphi_{or}) = 1 \quad (2)$$

Thus, one can determine the orientation of chaff elements by generating uniformly distributed random numbers in $[0, \pi]$ for θ_{or} and $[0, 2\pi]$ for φ_{or}. After performing the processes as (1) and (2), a simulation model of the chaff cloud can be established.

The subsequent kernel issue is how to make the physical model of the chaff corridor according to the simulation one. The simulation model is firstly divided into several parts on computer which can be seen in Fig.3. Then, a tooling is made according to the geometric information of these divided blocks to give a guide for chaff elements inserting. The design drawing of the chaff block and the tooling is shown in Fig.4. R is the diameter of the guiding holes which is slightly larger than the diameter r of the chaff element. L denotes the length of the chaff elements. For the facilitating convenience, the size of the block is chosen as 50 mm × 50 mm × 50 mm. The 3D showing of the chaff block and tooling is shown in Fig.5.

B. SCATTERING MATRIX MEASUREMENT

The scattering matrix, which is used to characterize the polaristic scattering properties of the chaff corridor, is crucial for
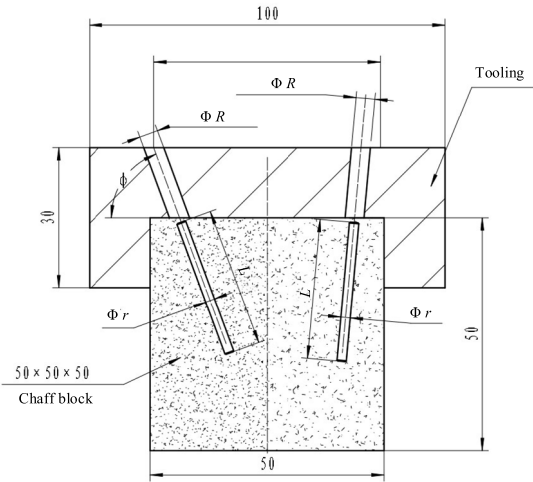
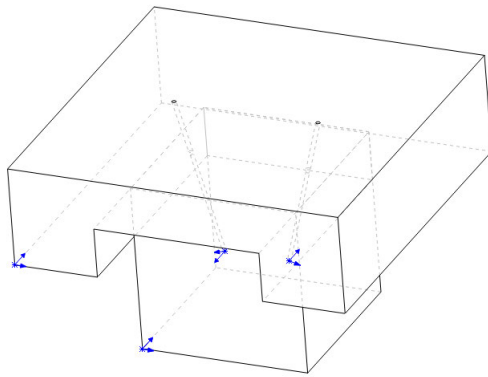**FIGURE 4.** The tooling for filberts insertion.

FIGURE 5. The 3D figure of tooling for filberts insertion.

target recognition. To study this, we use a plane EM wave incident upon a chaff corridor which can be written as

$$\vec{E}^{inc} = \hat{p}\vec{E}_p^{inc} + \hat{q}\vec{E}_q^{inc} \tag{3}$$

where, $\hat{p}$ and $\hat{q}$ are the unit coordinates vectors. In our topic, $\hat{p} = \hat{\theta}$ and $\hat{q} = \hat{\varphi}$ in spherical coordinate system. Similarly, the scattered field can be expressed as

$$\vec{E}^{sca} = \hat{p}\vec{E}_p^{sca} + \hat{q}\vec{E}_q^{sca} \tag{4}$$

and used to obtain

$$\begin{bmatrix} \vec{E}_p^{sca} \\ \vec{E}_q^{sca} \end{bmatrix} = \frac{e^{-jkR}}{R} \begin{bmatrix} S_{pp} & S_{pq} \\ S_{qp} & S_{qq} \end{bmatrix} \begin{bmatrix} \vec{E}_p^{inc} \\ \vec{E}_q^{inc} \end{bmatrix} = \frac{e^{-jkR}}{R} \mathbf{S}_{target}^{(0)} \begin{bmatrix} \vec{E}_p^{inc} \\ \vec{E}_q^{inc} \end{bmatrix} \tag{5}$$

where k is the wave number, R is the length of the radius vector $\vec{R}$ determined by the origin of the coordinate system and the observation point. $\mathbf{S}_{target}^{(0)}$ is the scattering matrix of the target. With this definition of the RCS

$$\sigma_{pq} = \lim_{R \to \infty} 4\pi R^2 \left| \vec{E}_p^{sca} \right|^2 \Big/ \left| \vec{E}_q^{inc} \right|^2 \tag{6}$$
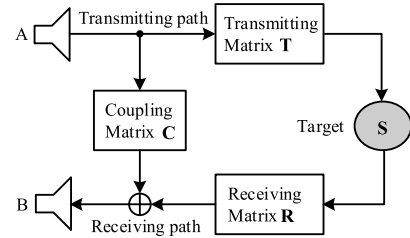

FIGURE 6. The model of signal transition in measurement.

one can rewrite (5) as

$$\begin{bmatrix} \vec{E}_p^{sca} \\ \vec{E}_q^{sca} \end{bmatrix} = \frac{1}{\sqrt{4\pi}R} \begin{bmatrix} \sqrt{\sigma_{pp}}e^{j\varphi_{pp}} & \sqrt{\sigma_{pq}}e^{j\varphi_{pq}} \\ \sqrt{\sigma_{qp}}e^{j\varphi_{qp}} & \sqrt{\sigma_{qq}}e^{j\varphi_{qq}} \end{bmatrix} \begin{bmatrix} \vec{E}_p^{inc} \\ \vec{E}_q^{inc} \end{bmatrix}$$

$$= \frac{1}{\sqrt{4\pi}R} \mathbf{S}_{target} \begin{bmatrix} \vec{E}_p^{inc} \\ \vec{E}_q^{inc} \end{bmatrix} \tag{7}$$

where the phase terms in matrix $\mathbf{S}_{target}$ indicate that the elements in the matrix are complex numbers. The signal flow chart of the measurement can be seen in Fig.6. One then can write the transfer function as [36]

$$\mathbf{U}_r = \left[\mathbf{C} + \mathbf{R}\mathbf{S}_{target}\mathbf{T} \right] \mathbf{U}_i \tag{8}$$

where the symbols $\mathbf{U}_i$ and $\mathbf{U}_r$ are the incident and scattered field vectors. Using this equation, the measured scattering matrix $\mathbf{S}_{measure}$ can be expressed as

$$\mathbf{S}_{measure} = \left[\mathbf{C} + \mathbf{R}\mathbf{S}_{target}\mathbf{T} \right] \tag{9}$$

It can be clearly seen from (9) that one cannot obtain the accurate scattering matrix $\mathbf{S}_{target}$ of the target under test without error compensation. In the following discussions, the method to determine matrix $\mathbf{C}$, $\mathbf{R}$, and $\mathbf{T}$ is presented using calibrators with known polaristic scattering matrix. Then the matrix $\mathbf{S}_{target}$ can be accessed according to (9).

To determine the matrix $\mathbf{C}$, One just needs to set matrix $\mathbf{S}_{target}$ as the zero matrix and get the following:

$$\mathbf{S}_{measure} = \begin{bmatrix} S_{m11}^{(0)} & S_{m12}^{(0)} \\ S_{m21}^{(0)} & S_{m22}^{(0)} \end{bmatrix} = \mathbf{C} = \begin{bmatrix} c_{11} & c_{12} \\ c_{21} & c_{22} \end{bmatrix} \tag{10}$$

Equation (10) holds when there is no scatter in the test region. One just needs to perform the test in a chamber without a target to obtain the matrix $\mathbf{C}$.

Secondly, the scattering matrix of a metal plate has the following form

$$\mathbf{S}_{target}^{plate} = \gamma_1 \begin{bmatrix} -1 & 0 \\ 0 & 1 \end{bmatrix} \tag{11}$$

where γ_1 is a complex constant. One can measure the metal plate and obtain

$$\begin{bmatrix} S_{m11}^{(1)} & S_{m12}^{(1)} \\ S_{m21}^{(1)} & S_{m22}^{(1)} \end{bmatrix} - \begin{bmatrix} c_{11} & c_{12} \\ c_{21} & c_{22} \end{bmatrix}$$

$$= \gamma_1 \begin{bmatrix} R_{11} & R_{12} \\ R_{21} & R_{22} \end{bmatrix} \begin{bmatrix} -1 & 0 \\ 0 & 1 \end{bmatrix} \begin{bmatrix} T_{11} & T_{12} \\ T_{21} & T_{22} \end{bmatrix} \tag{12}$$
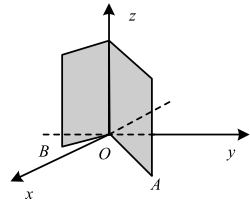
FIGURE 7. The model of rectangular dihedral reflector.

The scattering matrix of a metal sphere can be written as

$$\mathbf{S}_{target}^{ball} = \gamma_2 \begin{bmatrix} 1 & 0 \\ 0 & 1 \end{bmatrix} \quad (13)$$

where γ_2 is a complex constant. Similarly, one can measure the metal sphere and obtain

$$\begin{bmatrix} S_{m11}^{(2)} & S_{m12}^{(2)} \\ S_{m21}^{(2)} & S_{m22}^{(2)} \end{bmatrix} - \begin{bmatrix} c_{11} & c_{12} \\ c_{21} & c_{22} \end{bmatrix}$$
$$= \gamma_2 \begin{bmatrix} R_{11} & R_{12} \\ R_{21} & R_{22} \end{bmatrix} \begin{bmatrix} 1 & 0 \\ 0 & 1 \end{bmatrix} \begin{bmatrix} T_{11} & T_{12} \\ T_{21} & T_{22} \end{bmatrix} \quad (14)$$

Now, let us consider a rectangular dihedral reflector which is denoted in Fig.7. Vector $\overrightarrow{OA}$ can be written as

$$\frac{\overrightarrow{OA}}{\left|\overrightarrow{OA}\right|} = \frac{1}{\sqrt{2}} \left(\hat{x} + \hat{y}\right) \quad (15)$$

where $\angle AOB = 90°$. If one rotates the rectangular dihedral reflector around the x axis with angle θ, the scattering matrix of the rectangular dihedral reflector can be express as

$$\mathbf{S}_{target}^{rdr} = \gamma_3 \begin{bmatrix} \cos 2\theta & \sin 2\theta \\ \sin 2\theta & -\cos 2\theta \end{bmatrix} \quad (16)$$

For example, when setting $\theta = \pi/4$, the scattering matrix can be then written as

$$\mathbf{S}_{target}^{rdr} = \gamma_3 \begin{bmatrix} 0 & 1 \\ 1 & 0 \end{bmatrix} \quad (17)$$

Similar works can be done and obtain

$$\begin{bmatrix} S_{m11}^{(3)} & S_{m12}^{(3)} \\ S_{m21}^{(3)} & S_{m22}^{(3)} \end{bmatrix} - \begin{bmatrix} c_{11} & c_{12} \\ c_{21} & c_{22} \end{bmatrix}$$
$$= \gamma_3 \begin{bmatrix} R_{11} & R_{12} \\ R_{21} & R_{22} \end{bmatrix} \begin{bmatrix} \cos 2\theta & \sin 2\theta \\ \sin 2\theta & -\cos 2\theta \end{bmatrix} \begin{bmatrix} T_{11} & T_{12} \\ T_{21} & T_{22} \end{bmatrix} \quad (18)$$

If one introduces the matrix **G** to represent the results in the right hand of (12), (14) and (18). One gets

$$\mathbf{G}^{(1)} = \begin{bmatrix} S_{m11}^{(1)} & S_{m12}^{(1)} \\ S_{m21}^{(1)} & S_{m22}^{(1)} \end{bmatrix} - \begin{bmatrix} c_{11} & c_{12} \\ c_{21} & c_{22} \end{bmatrix} \quad (19)$$

$$\mathbf{G}^{(2)} = \begin{bmatrix} S_{m11}^{(2)} & S_{m12}^{(2)} \\ S_{m21}^{(2)} & S_{m22}^{(2)} \end{bmatrix} - \begin{bmatrix} c_{11} & c_{12} \\ c_{21} & c_{22} \end{bmatrix} \quad (20)$$

$$\mathbf{G}^{(3)} = \begin{bmatrix} S_{m11}^{(3)} & S_{m12}^{(3)} \\ S_{m21}^{(3)} & S_{m22}^{(3)} \end{bmatrix} - \begin{bmatrix} c_{11} & c_{12} \\ c_{21} & c_{22} \end{bmatrix} \quad (21)$$

Therefore, (12) and (14) can be rewritten as

$$\mathbf{G}^{(1)} = \begin{bmatrix} G_{11}^{(1)} & G_{12}^{(1)} \\ G_{21}^{(1)} & G_{22}^{(1)} \end{bmatrix}$$
$$= \gamma_1 \begin{bmatrix} R_{11} & R_{12} \\ R_{21} & R_{22} \end{bmatrix} \begin{bmatrix} -1 & 0 \\ 0 & 1 \end{bmatrix} \begin{bmatrix} T_{11} & T_{12} \\ T_{21} & T_{22} \end{bmatrix} \quad (22)$$

$$\mathbf{G}^{(2)} = \begin{bmatrix} G_{11}^{(2)} & G_{12}^{(2)} \\ G_{21}^{(2)} & G_{22}^{(2)} \end{bmatrix}$$
$$= \gamma_2 \begin{bmatrix} R_{11} & R_{12} \\ R_{21} & R_{22} \end{bmatrix} \begin{bmatrix} 1 & 0 \\ 0 & 1 \end{bmatrix} \begin{bmatrix} T_{11} & T_{12} \\ T_{21} & T_{22} \end{bmatrix} \quad (23)$$

$$\mathbf{G}^{(3)} = \begin{bmatrix} G_{11}^{(3)} & G_{12}^{(3)} \\ G_{21}^{(3)} & G_{22}^{(3)} \end{bmatrix}$$
$$= \gamma_3 \begin{bmatrix} R_{11} & R_{12} \\ R_{21} & R_{22} \end{bmatrix} \begin{bmatrix} \cos 2\theta & \sin 2\theta \\ \sin 2\theta & -\cos 2\theta \end{bmatrix} \begin{bmatrix} T_{11} & T_{12} \\ T_{21} & T_{22} \end{bmatrix} \quad (24)$$

We can solve **R** from (23) and subtitle it into (22), yields

$$\begin{bmatrix} R_{11} & R_{12} \\ R_{21} & R_{22} \end{bmatrix} = \frac{1}{\gamma_2} \mathbf{G}^{(2)} \begin{bmatrix} T_{11} & T_{12} \\ T_{21} & T_{22} \end{bmatrix}^{-1} \quad (25)$$

and

$$\begin{bmatrix} T_{11} & T_{12} \\ T_{21} & T_{22} \end{bmatrix} \left(\mathbf{G}^{(2)}\right)^{-1} \mathbf{G}^{(1)}$$
$$= \frac{\gamma_2}{\gamma_1} \begin{bmatrix} -1 & 0 \\ 0 & 1 \end{bmatrix} \begin{bmatrix} T_{11} & T_{12} \\ T_{21} & T_{22} \end{bmatrix} \quad (26)$$

After algebraic operations, we can define matrix as

$$\mathbf{D}_1 = \begin{bmatrix} d_{11}^{(1)} & d_{12}^{(1)} \\ d_{21}^{(1)} & d_{22}^{(1)} \end{bmatrix} = \begin{bmatrix} G_{11}^{(2)} & G_{12}^{(2)} \\ G_{21}^{(2)} & G_{22}^{(2)} \end{bmatrix}^{-1} \begin{bmatrix} G_{11}^{(1)} & G_{12}^{(1)} \\ G_{21}^{(1)} & G_{22}^{(1)} \end{bmatrix} \quad (27)$$

Then, one can obtain

$$\begin{cases} d_{11}^{(1)} T_{11} + d_{21}^{(1)} T_{12} = -\dfrac{\gamma_1}{\gamma_2} T_{11} \\ d_{12}^{(1)} T_{11} + d_{22}^{(1)} T_{12} = -\dfrac{\gamma_1}{\gamma_2} T_{12} \end{cases} \quad (28)$$

Thus,

$$\left(\frac{T_{11}}{T_{12}}\right)^2 d_{12}^{(1)} + \left(d_{22}^{(1)} - d_{11}^{(1)}\right)\frac{T_{11}}{T_{12}} - d_{21}^{(1)} = 0 \quad (29)$$

the solution of (29) can be obtained, say ξ_1. Similar works can be performed and get

$$\begin{cases} d_{11}^{(1)} T_{21} + d_{12}^{(1)} T_{22} = \dfrac{\gamma_1}{\gamma_2} T_{21} \\ d_{21}^{(1)} T_{21} + d_{22}^{(1)} T_{22} = \dfrac{\gamma_1}{\gamma_2} T_{22} \end{cases} \quad (30)$$

Thus,

$$\left(\frac{T_{21}}{T_{22}}\right)^2 d_{12}^{(1)} + \left(d_{22}^{(1)} - d_{11}^{(1)}\right)\frac{T_{21}}{T_{22}} - d_{21}^{(1)} = 0 \quad (31)$$

the solution of (31) can be obtained, say ξ_2. Next, by using (16), one can obtain

$$\mathbf{D}_2 = \begin{bmatrix} d_{11}^{(2)} & d_{12}^{(2)} \\ d_{21}^{(2)} & d_{22}^{(2)} \end{bmatrix} = \begin{bmatrix} G_{11}^{(3)} & G_{12}^{(3)} \\ G_{21}^{(3)} & G_{22}^{(3)} \end{bmatrix}^{-1} \begin{bmatrix} G_{11}^{(1)} & G_{12}^{(1)} \\ G_{21}^{(1)} & G_{22}^{(1)} \end{bmatrix} \quad (32)$$

and thus,

$$\frac{d_{11}^{(2)}T_{11} + d_{21}^{(2)}T_{12}}{d_{12}^{(2)}T_{11} + d_{22}^{(2)}T_{12}} = \frac{T_{11}\cos 2\theta + T_{21}\sin 2\theta}{T_{12}\sin 2\theta + T_{22}\cos 2\theta} \quad (33)$$

and

$$\frac{d_{11}^{(2)}T_{21} + d_{21}^{(2)}T_{22}}{d_{12}^{(2)}T_{21} + d_{22}^{(2)}T_{22}} = \frac{T_{11}\sin 2\theta - T_{21}\cos 2\theta}{T_{12}\sin 2\theta - T_{22}\cos 2\theta} \quad (34)$$

Deriving from (33) and (34), one can get

$$\tan 2\theta = \frac{T_{11}^2 d_{12}^{(2)} - T_{11}T_{22}d_{11}^{(2)} - T_{11}T_{12}d_{22}^{(2)} - T_{12}T_{22}d_{21}^{(2)}}{T_{12}^2 d_{21}^{(2)} + T_{11}T_{12}d_{11}^{(2)} - T_{11}T_{21}d_{12}^{(2)} - T_{12}T_{21}d_{22}^{(2)}} \quad (35)$$

$$\tan 2\theta = \frac{T_{11}^2 d_{12}^{(2)} - T_{22}^2 d_{21}^{(2)} + T_{21}T_{22}\left(d_{22}^{(2)} - d_{11}^{(2)}\right)}{T_{11}T_{21}d_{12}^{(2)} - T_{12}T_{21}d_{11}^{(2)} + T_{11}T_{22}d_{22}^{(2)} - T_{12}T_{22}d_{21}^{(2)}} \quad (36)$$

Then, one can let the right hand term of (35) equal to that of (36) and obtain

$$\frac{T_{11}^2 d_{12}^{(2)} - T_{11}T_{22}d_{11}^{(2)} - T_{11}T_{12}d_{22}^{(2)} - T_{12}T_{22}d_{21}^{(2)}}{T_{12}^2 d_{21}^{(2)} + T_{11}T_{12}d_{11}^{(2)} - T_{11}T_{21}d_{12}^{(2)} - T_{12}T_{21}d_{22}^{(2)}}$$
$$= \frac{T_{11}^2 d_{12}^{(2)} - T_{22}^2 d_{21}^{(2)} + T_{21}T_{22}\left(d_{22}^{(2)} - d_{11}^{(2)}\right)}{T_{11}T_{21}d_{12}^{(2)} - T_{12}T_{21}d_{11}^{(2)} + T_{11}T_{22}d_{22}^{(2)} - T_{12}T_{22}d_{21}^{(2)}} \quad (37)$$

Then, one gets the polynomial equation

$$A\left(\frac{T_{21}}{T_{11}}\right)^3 + B\left(\frac{T_{21}}{T_{11}}\right)^2 + C\left(\frac{T_{21}}{T_{11}}\right) + D = 0 \quad (38)$$

where the constants in (38) are written as

$$A = -\left(d_{12}^{(2)} + \frac{d_{22}^{(2)}}{\xi_1}\right) \cdot \frac{d_{21}^{(2)} + \xi_2\left(d_{11}^{(2)} - d_{22}^{(2)}\right)}{\xi_2^2} \quad (39)$$

$$C = d_{12}^{(2)}\left(d_{12}^{(2)} + \frac{d_{22}^{(2)}}{\xi_1}\right)$$
$$+ \left(d_{12}^{(2)} - \frac{d_{22}^{(2)}}{\xi_1}\right) \cdot \left(d_{21}^{(2)} - \frac{d_{11}^{(2)}}{\xi_1} + \frac{d_{22}^{(2)}}{\xi_2} - \frac{d_{21}^{(2)}}{\xi_1\xi_2}\right) \quad (40)$$

$$B = \left[d_{21}^{(2)} + \frac{\xi_2 d_{22}^{(2)} - \xi_2 d_{11}^{(2)} - d_{21}^{(2)}}{\xi_1\xi_2}\right]$$
$$\cdot \left[\frac{\xi_1 d_{11}^{(2)} + d_{21}^{(2)}}{\xi_1^2} \cdot \frac{\xi_2\left(d_{11}^{(2)} - d_{22}^{(2)}\right) + d_{21}^{(2)}}{\xi_2^2} - \frac{\xi_1 d_{11}^{(2)} + d_{21}^{(2)}}{\xi_1\xi_2}\right] \quad (41)$$

$$D = -d_{12}^{(2)} \cdot \frac{d_{11}^{(2)}\xi_1 + d_{21}^{(2)}}{\xi_1^2} \quad (42)$$

with (29), (31) and (38), the matrix **T** is determined. The matrix **R** can be subsequently determined by (25). So the scattering matrix of the target can be written as

$$\mathbf{S}_{\text{target}} = (1/\gamma_2) \cdot \mathbf{T}\left(\mathbf{G}^{(2)}\right)^{-1}(\mathbf{S}_{measure} - \mathbf{C})\,\mathbf{T}^{-1} \quad (43)$$

from (43), one can obtain the scattering matrix of the target just performing basic matrix operations. It should be noted that one or two amplifiers are added into the measurement system when needed. Thus, the calibration and measurement processes mentioned above need to be conducted considering the amplifiers as a part of the system. When the system settings are changed, the calibration process must be re-conducted.

C. EXTINCTION COEFFICIENTS MEASUREMENT

The extinction coefficient κ refers to the energy attenuation rate of the EM wave passing through the chaff corridor. The wave number k of a homogeneous wave may be written as

$$k = \frac{\omega}{c}N = \frac{\omega}{c}(n + i\kappa) \quad (44)$$

where c is the speed and ω is angular frequency of the wave. N is so called the complex refractive index. Using this formula, a plane homogeneous wave, transit along $\hat{z}$, has the form

$$\vec{E}_c = \vec{E}_0 \exp\left(-\frac{2\pi\kappa z}{\lambda}\right)\exp\left(\frac{i2\pi nz}{\lambda} - i\omega t\right) \quad (45)$$

As the wave traverses the chaff corridor, the power is exponentially attenuated

$$P_L = P_0 e^{-\alpha L} \quad (46)$$

in this equation, P_0 and P_L are the power obtained at $z = 0$ and $z = L$, respectively. α is the absorption coefficient with the form of

$$\alpha = \frac{4\pi\kappa}{\lambda} \quad (47)$$

where λ is the wavelength. Then, α, and hence κ, can be obtained in principle from the relation described in the next equation:

$$\alpha L = \frac{4\pi\kappa}{\lambda}L = \ln\frac{P_0}{P_L} \quad (48)$$

The scattering model of a block of the chaff corridor can be reported in Fig.8.

It is obvious that the power at the two surfaces of the chaff corridor is hard to be detected. A more convenient way to estimate the extinction coefficient is measuring the reflectance and transmittance of the chaff corridor. We denote the reflectance and transmittance of the chaff corridor as R and T, respectively. After some algebraic manipulations, we obtain the following equation:

$$\frac{1 - R}{T} = \exp\left(\frac{4\pi L}{\lambda}\kappa\right) \quad (49)$$

The next important issue that needs to be addressed is how to perform measurements to obtain the reflectance and transmittance of the chaff corridor. The "comparison" method is adopted. At first, a plane with known reflectance is tested as shown Fig.9 using antennas A and B. By noting the transmitting power as P_t^0, and the receiving power as P_r^0, we obtain

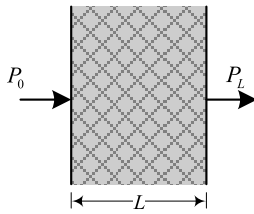$$\Gamma_0 = \xi_1 \frac{P_r^0}{P_t^0} \quad (50)$$

FIGURE 8. The figure of the energy passing through a test range.

FIGURE 9. The scenario of reflectance and transmittance measurement.

where Γ_0 is the reflectance of the plane and ξ_1 is the calibration coefficient of the measurement system which will not change under the same test condition. Secondly, the test of a chaff corridor which has the same area with the plane is performed under the same condition. Thus, we obtain

$$\Gamma_c = \xi_1 \frac{P_c}{P_t^0} \qquad (51)$$

where Γ_c and P_c^0 are the reflectance and reflected power of the chaff corridor, respectively. From the division of (50) and (51), we get

$$R = \frac{\Gamma_0 P_c}{P_r^0} \qquad (52)$$

The experimental determination of the transmittance of the chaff corridor can be performed in the same way. Instead of arranging an object with known transmittance, we place an imaginary standard material within the test region, i.e. the air. In other words, we measure the power with the absence of the chaff corridor. Then we can obtain

$$T_0 = \xi_2 \frac{P_r^0}{P_t^0} \qquad (53)$$

where ξ_2 is calibration coefficient of the measurement system. The chaff corridor is tested and thus we get below:

$$T_c = \xi_2 \frac{P_c}{P_t^0} \qquad (54)$$

After some algebraic operation, we obtain:

$$T = \frac{T_0 P_c}{P_r^{0.}} \qquad (55)$$

If one wants to obtain the polaristic extinction coefficient of the chaff corridor, the polaristic reflectance and transmittance should be probed. One rotates two antennas simultaneously to form different polaristic angles. Meanwhile, the polaristic reflectance and transmittance of the standard materials (or objects) under the same incident and received conditions are sampled to set a reference for the extinction measurement of the chaff corridor. The test scenario is shown in Fig.9.

D. THE MEASUREMENT SYSTEM
1) SCATTERING MATRIX MEASUREMENT FACILITIES
The scattering matrix measurements of the chaff corridor are performed in the radio anechoic chamber which can reduce unnecessary reflected power. The facilities in our
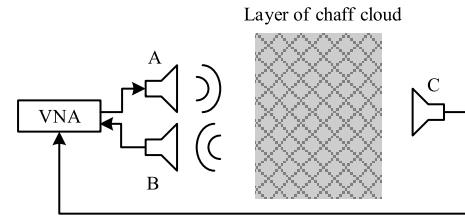
lab operate at frequencies from 18 to 24 GHz. The stepped frequency measurement system is adopted which can realize a wide-total-bandwidth and full-polarization measurements. The block diagram is shown in Fig.10. A pair of horn antennas are used as the transmitting and receiving devices that realize 360-degree angle polarization measurements without losing of focus. In practical measurements, the reflected power level of the object is not always very high, which causes difficulty in reflected signal capture. Therefore, two amplifiers are adopted associating with the transmitting and receiving antennas to improve the dynamic range of the measurement system. The central computer of the system is set as the "commander". It controls the vector network analyzer (VNA) and turntable to perform the measurements. The turntable is located on the opposite side of the antennas. The object under test, i.e., the model of the chaff corridor, is placed on the upper surface of the turntable which can rotate around the plumb line. To restrain the EM scattering of the turntable, an absorbing wall is built in front of the turntable. Besides, a microwave absorbing board is set between two antennas to suppress the direct-transmission noise.

Based on the test principals and facilities, the test has four steps: First, the measurement system runs for about 30 minutes before test. Secondly, the height of the antenna is adjusted to ensure that the centers of the target and antennas are located within the same plane and aligned. Thirdly, the system is calibrated using standard calibrators as described in the previous sections. To reduce the multipath effect, the virtual time-domain gating technique is used. Fourthly, after the calibration, all of the facilities and variables in the software are fixed and the object is put back on the turntable. The rotation angle of each antenna is set according to the test plan. The central computer controls the turntable to rotate for each step. In those steps, the antennas emit the stepped frequency signals and receive the echo. The software gives the S-parameters at every frequency point, every azimuth angle, and every set of the antennas' polaristic angles. These collected data are used to determine the scattering matrix of the chaff corridor. The block diagram of the measurement process is illustrated in Fig.11.

2) THE FACILITIES FOR EXTINCTION COEFFICIENT MEASUREMENT
The extinction coefficient is always used to describe the ability of the EM wave passing through the chaff corridor. The measurements of the extinction coefficients of the chaff
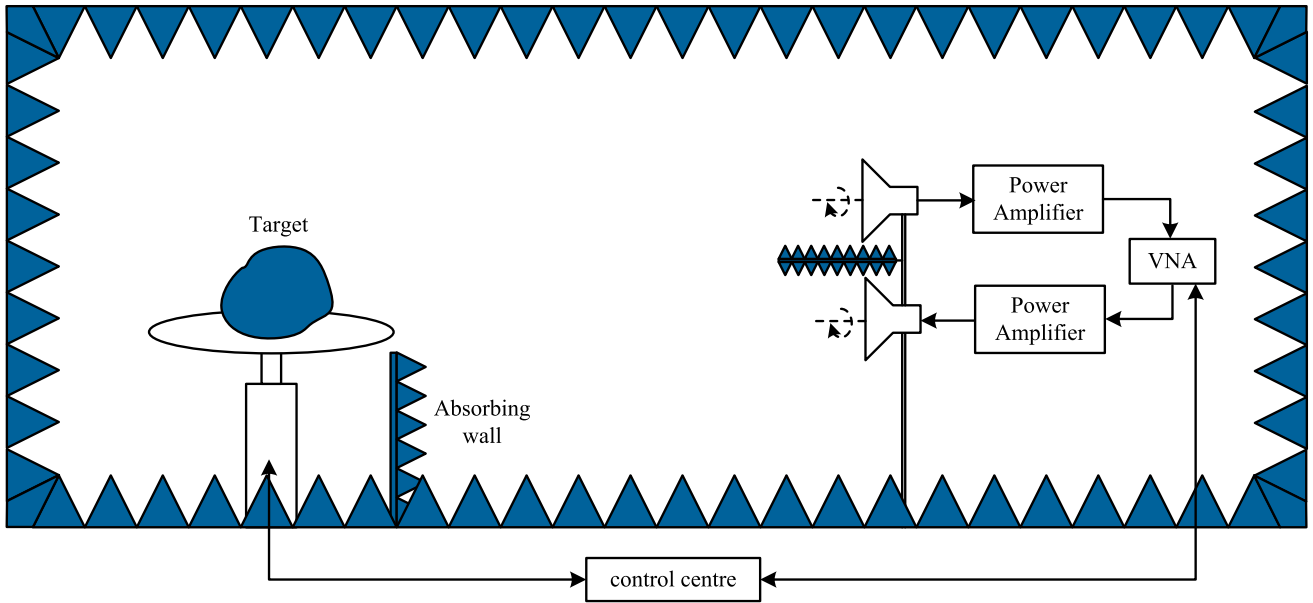
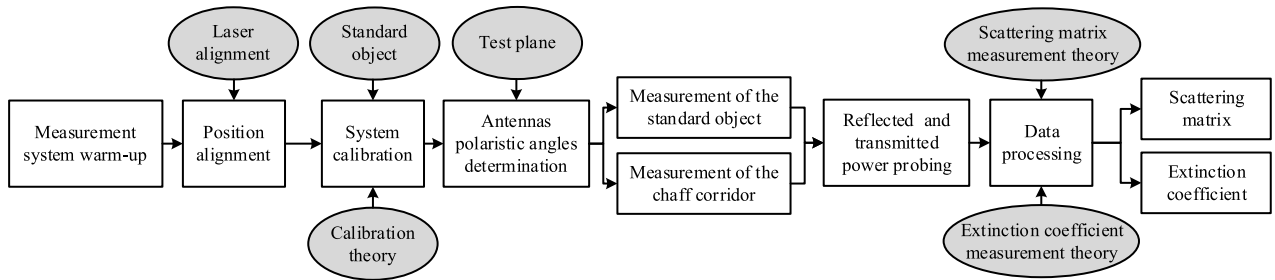**FIGURE 10.** The block diagram of the measurement system.

FIGURE 11. The block diagram of the measurement process.

corridor are still performed in the chamber. The instruments operate at frequency from 18 to 24 GHz. The waveform of the emitting signal is also selected as the stepped-frequency continuous-wave. The block diagram of this test mode is shown in Fig.12. The target under test is arranged between two horn antennas. A low-RCS pylon is installed to support the target. At this time, the power amplifier is optional. When the reflected power level of the target is high enough, it allows one or two of the amplifiers to be turned off.

The test has several steps: First, the measurement system is installed and the laser positioning system is used to make sure the two antennas are center aligned. Next, the system is calibrated. Meanwhile, the reflected and transmitted power is probed. If this power level does not meet the testing criterion, power amplifiers are added into the circuit. Then, the transmitted and received power of the EM field with the absence of the target, and later with the presence of the chaff corridor are recorded. At the same time, the thickness of the chaff corridor is measured. Finally, data are processed by the central computer to obtain the extinction coefficients of the chaff corridors. In addition, the angle of two horn antennas is adjusted to obtain the polaristic extinction coefficients of

the chaff corridor. The block diagram of the measurement process is illustrated in Fig.11.

III. MEASUREMENT AND ANALYSIS

In the prior sections, we have addressed the theory how to determine the scattering matrix and the extinction coefficient of the chaff cloud by experiments. In this section, we first perform the validation experiments to confirm the methods presented in this article. Then, the scattering matrixes and extinction coefficients of different types of the chaff corridors under different polaristic angles and frequencies are determined. Finally, some useful conclusions are given. The photos of the test facilities are shown in Fig.13 where (a) and (b) show the test scenarios of the scattering matrix measurement, while (c) and (d) show the test scenarios of the extinction coefficient measurement.

A. ALGORITHM VALIDATION

In this part, we focus on the validation of the measurement method presented in Section II. At the beginning of this part, two typical objects (metallic cubic and corner reflector) are tested in the chamber. As a contrast, the theoretical scattering
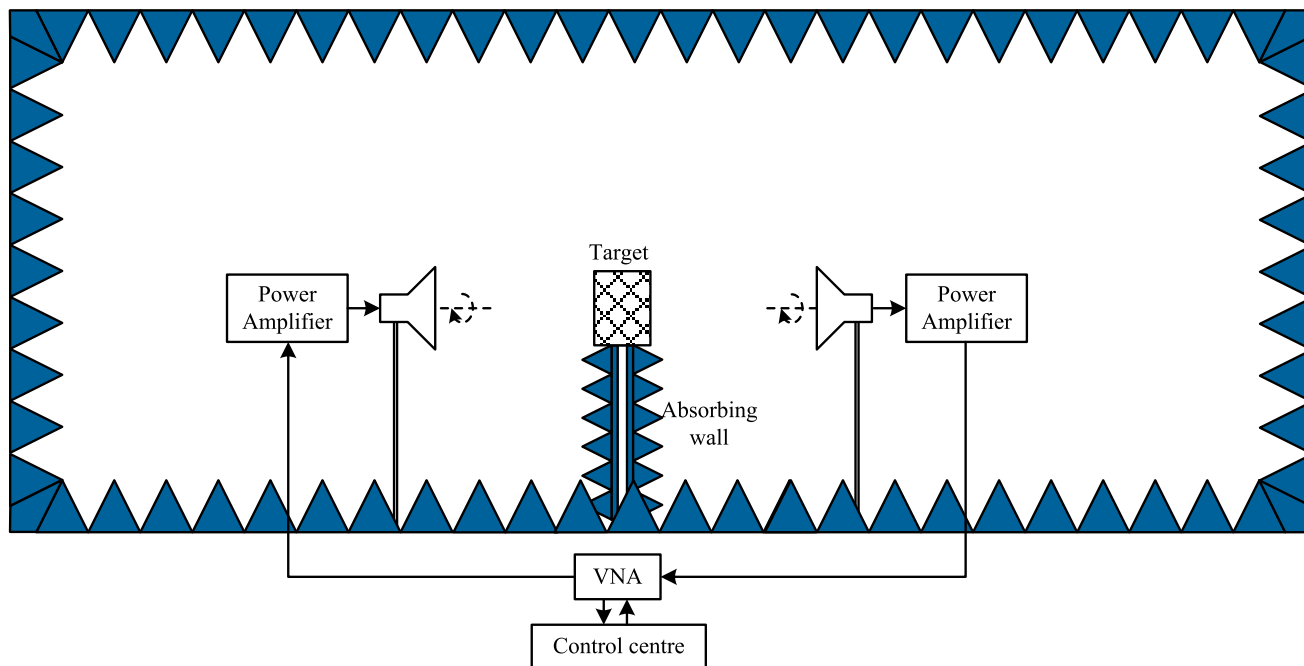
FIGURE 12. The block diagram of the measurement system.

TABLE 1. The scattering matrices of typical objects.

Case	Model picture	Simulation and measurement	Case	Model picture	Simulation and measurement
1		(1) Simulation result: $\begin{bmatrix} 1.00 + 0.00i & 0.00 - 0.00i \\ 0.00 + 0.00i & 1.00 + 0.00i \end{bmatrix}$ (2) Measurement result: $\begin{bmatrix} 1.00 + 0.00i & 0.05 + 0.00i \\ 0.03 + 0.02i & 1.00 + 0.00i \end{bmatrix}$	2		(1) Simulation result: $\begin{bmatrix} 1.00 + 0.00i & 0.00 + 0.00i \\ 0.00 + 0.00i & 0.86 + 0.74i \end{bmatrix}$ (2) Measurement result: $\begin{bmatrix} 1.00 + 0.00i & 0.00 - 0.02i \\ 0.01 + 0.00i & 1.00 + 0.00i \end{bmatrix}$
3		(1) Simulation result: $\begin{bmatrix} 1.00 + 0.00i & 0.00 - 0.00i \\ 0.00 + 0.00i & 1.00 + 0.00i \end{bmatrix}$ (2) Measurement result: $\begin{bmatrix} 1.00 + 0.00i & 0.03 + 0.01i \\ 0.04 + 0.03i & 1.00 + 0.00i \end{bmatrix}$	4		(1) Simulation result: $\begin{bmatrix} 1.00 + 0.00i & -0.74 - 0.58i \\ 1.48 + 0.51i & 1.19 + 0.41i \end{bmatrix}$ (2) Measurement result: $\begin{bmatrix} 1.00 + 0.00i & -0.53 - 0.26i \\ 1.39 + 0.55i & 1.05 + 0.39i \end{bmatrix}$

Notes: the simulation and experimental constitutions: Case 1: cubic, $f = 20$ GHz, incident direction $\theta=0°$, $\varphi=0°$. Case 2: cubic, $f = 18$ GHz, incident direction $\theta=0°$, $\varphi=75°$.
Case 3: corner reflector, $f = 21$ GHz, incident direction $\theta=90°$, $\varphi=45°$. Case 4: corner reflector, $f = 21$ GHz, incident direction $\theta=63°$, $\varphi=50°$.

matrices of these objects are obtained in the commercial software under the same conditions. Then, three materials are utilized to verify the method of extinction coefficient extraction. Different from the measurements of the scattering matrix, the validation processes of the extinction coefficient extraction are all conducted in the commercial simulation software. Since we do not have enough types of materials with known material parameters, especially very large or small extinction coefficient materials.

To verify the scattering matrix method presented in the previous section, the standard objects, i.e., cubic and corner reflector, are adopted for testing. The geometric models and

corresponding coordinates system are illustrated in Fig.14. These objects are all perfect electric conductors (PECs). When conducting the software simulations on computer and measurements in the chamber, they all respect the same coordinate systems and test conditions. For convenience, the spherical coordinate systems are defined cooperating with the Cartesian coordinate system defined in Fig.14 (a) and (b). The simulation and experimental conditions are presented in the notes part of Table 1. The corresponding results are also reported in Table 1. It can be seen from the table that the scattering matrices obtained by the method presented in this article have a good agreement with the theoretical ones.

TABLE 2. The extraction coefficients of typical materials.

	Case 1	Case 2	Case 3	Case 4	Case 5	Case 6
Simulation	8.50	8.50	21.30	21.30	125.00	137.00
Measurement	8.39	8.57	22.19	21.01	121.35	134.81

Notes: the simulation and experimental constitutions: incident direction $\theta=0°$, $\varphi=0°$. Case 1: material-1, f = 20 GHz, thinness 10 cm, Case 2: material-1, f = 20 GHz, thinness 15 cm. Case 3: material-2, f = 18 GHz, thinness 5 cm. Case 4: material-2, f = 22 GHz, thinness 15 cm. Case 5: material-3, f = 20 GHz, thinness 3 cm. Case 6: material-3, f = 15 GHz, thinness 5 cm
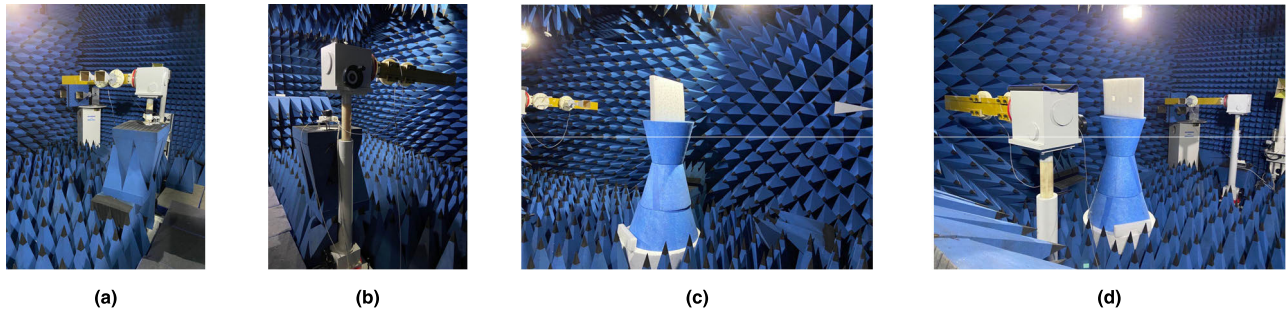

FIGURE 13. The measurement facilities in chamber. (a) and (b) are the facilities for scattering matrix measurements. (c) and (d) are the facilities for extinction coefficient measurements.

However, when the reflected power level of the cross-polarized mode is low, the prediction errors increase. The possible reason is that the antennas we used in the test are not pure linear polarized and the physical model of the standard object cannot be arranged strictly according to the simulation one. Besides, the measurement accuracy of the scattering matrix of the standard objects decreases with the increasing frequencies. This is mainly because the phase detection errors caused by the positioning error of the standard object and facilities increase.
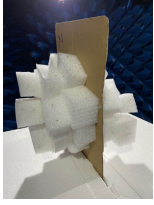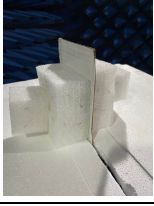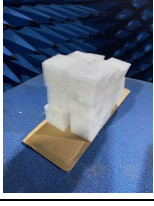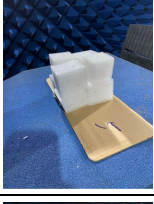
We now deal with the validation of the method for extinction coefficients measurement. The coordinate system of the simulations is shown in Fig.14 (c). The origin is located at the geometric center of the material block. In the software simulations, two virtual probes are set on both sides of the material along the direction of the incident wave, which is similar to the scenario in Fig.13 (d). Then, the data is collected and processed following the method presented in Section II. The simulation conditions are given in the notes part following Table 2. The extinction coefficients obtained by the method presented in Section II (we treated then as the "measurement" results) and through the calculation from the material parameters (we treat them as the "simulation" results) are reported in Table 2. From these results, it can be found that the extinction coefficients predicted by the method presented in this article are very close to the true values of the materials. We also find that larger prediction errors occur when the thickness of the material is smaller and the operating wavelength of the radar is larger. The possible reason is that an object can be considered as a layer of material more reasonably when they are electrical large

relative to the operating wavelength of the radar. Besides, from Case 1 and Case 2 in Table 2 we also find that the theatrical values of the extinction coefficient of the chaff corridor are not changing with the thickness of the material in our simulations. Because the extinction coefficient is only determined by the electric attributes of the material [37], [38]. Overall, the validation experiments performed in this part verify the scattering matrix and extinction coefficient measurement methods presented in this article.

B. SCATTERING MATRIX MEASUREMENTS

In the scattering matrix measurements, six models are tested. The pictures of these models can be found in the second column of Table 3. The chaff models consist of many blocks which are made according to the simulations. The size of each block is 5 cm × 5 cm × 5 cm. There are 24 elements involved in each block. The length of the chaff elements is selected as 3 cm. For Case 1 and Case 3, the model of the chaff cloud is formed as ellipsoid. Three axes lengths of Case 1 are 13 cm, 13 cm, and 25 cm. Three axes lengths of Case 3 are 8 cm, 8 cm, and 17 cm. For Case 2, an irregular shaped chaff cloud model is made. To investigate the EM scattering properties of different types of chaff cloud, Case 4, Case 5, and Case 6 give the chaff model shaped as cuboid. For Case 4, Case 5, and Case 6, the edge lengths of the chaff cloud are 15 cm × 15 cm × 10 cm, 10 cm × 10 cm × 10 cm, and 15 cm × 10 cm × 5 cm, respectively. The operating frequency of the measurement system ranges from 20 GHz to 24 GHz. The transmitting and receiving antennas are both the standard-Gain horn antennas.

TABLE 3. Results of the scattering matrix measurements.

Case	Model picture	f	0°	90°	180°	270°
1		20	$\begin{bmatrix} 1.00+0.00i & -0.281-0.32i \\ -0.29-0.35i & 1.020+0.08i \end{bmatrix}$	$\begin{bmatrix} 1.00+0.00i & 0.47+0.12i \\ 0.43+0.13i & 1.09+0.02i \end{bmatrix}$	$\begin{bmatrix} 1.00+0.00i & -0.36+0.04i \\ -0.34+0.01i & 0.96+0.03i \end{bmatrix}$	$\begin{bmatrix} 1.00+0.00i & 0.00+0.02i \\ 0.01+0.00i & 1.02+0.07i \end{bmatrix}$
		22	$\begin{bmatrix} 1.00+0.00i & -0.01-0.28i \\ -0.00-0.25i & 0.90-0.04i \end{bmatrix}$	$\begin{bmatrix} 1.00+0.00i & -0.07+0.11i \\ -0.08+0.12i & 1.05+0.01i \end{bmatrix}$	$\begin{bmatrix} 1.00+0.00i & -0.24+0.16i \\ -0.26+0.15i & 1.07+0.02i \end{bmatrix}$	$\begin{bmatrix} 1.00+0.00i & 0.04-0.01i \\ 0.04-0.01i & 0.91-0.03i \end{bmatrix}$
		24	$\begin{bmatrix} 1.00+0.00i & -0.18+0.01i \\ -0.16+0.02i & 0.95-0.07i \end{bmatrix}$	$\begin{bmatrix} 1.00+0.00i & -0.06-0.01i \\ -0.05-0.01i & 0.91+0.03i \end{bmatrix}$	$\begin{bmatrix} 1.00+0.00i & -1.09+2.11i \\ -0.98+2.24i & 0.99-0.03i \end{bmatrix}$	$\begin{bmatrix} 1.00+0.00i & 0.00+0.01i \\ 0.00+0.01i & 1.03-0.01i \end{bmatrix}$
2		20	$\begin{bmatrix} 1.00+0.00i & 1.73-0.05i \\ 1.57-0.11i & 1.10+0.04i \end{bmatrix}$	$\begin{bmatrix} 1.00+0.00i & -0.07-0.18i \\ -0.06-0.17i & 0.93+0.01i \end{bmatrix}$	$\begin{bmatrix} 1.00+0.00i & 0.06-0.06i \\ 0.06-0.06i & 1.05+0.02i \end{bmatrix}$	$\begin{bmatrix} 1.00+0.00i & -0.01+0.05i \\ -0.01+0.04i & 1.04+0.03i \end{bmatrix}$
		22	$\begin{bmatrix} 1.00+0.00i & -0.57+0.37i \\ -0.61+0.35i & 1.04+0.02i \end{bmatrix}$	$\begin{bmatrix} 1.00+0.00i & -0.02-0.09i \\ -0.03-0.09i & 1.10-0.08i \end{bmatrix}$	$\begin{bmatrix} 1.00+0.00i & 1.12+0.82i \\ 1.09+0.84i & 1.09-0.01i \end{bmatrix}$	$\begin{bmatrix} 1.00+0.00i & -0.14+0.00i \\ -0.15+0.01i & 1.06-0.03i \end{bmatrix}$
		24	$\begin{bmatrix} 1.00+0.00i & 0.37+0.78i \\ 0.28+0.79i & 1.12-0.00i \end{bmatrix}$	$\begin{bmatrix} 1.00+0.00i & -0.01-0.02i \\ -0.01-0.02i & 1.04-0.08i \end{bmatrix}$	$\begin{bmatrix} 1.00+0.00i & 0.61+0.70i \\ 0.56+0.66i & 1.06+0.00i \end{bmatrix}$	$\begin{bmatrix} 1.00+0.00i & -0.01+0.00i \\ -0.01+0.00i & 0.98+0.01i \end{bmatrix}$
3		20	$\begin{bmatrix} 1.00+0.00i & -0.53-0.66i \\ -0.56-0.65i & 1.02-0.01i \end{bmatrix}$	$\begin{bmatrix} 1.00+0.00i & 0.01-0.00i \\ 0.01-0.00i & 1.06+0.01i \end{bmatrix}$	$\begin{bmatrix} 1.00+0.00i & 0.56+0.92i \\ 0.54+1.03i & 0.99-0.02i \end{bmatrix}$	$\begin{bmatrix} 1.00+0.00i & -0.38+0.17i \\ -0.35+0.15i & 0.95+0.08i \end{bmatrix}$
		22	$\begin{bmatrix} 1.00+0.00i & 1.14-2.94i \\ 1.24-2.94i & 0.92-0.04i \end{bmatrix}$	$\begin{bmatrix} 1.00+0.00i & 2.64-10.00i \\ 4.09-10.02i & 0.95+0.02i \end{bmatrix}$	$\begin{bmatrix} 1.00-0.00i & 0.18-0.01i \\ 0.19-0.01i & 1.05-0.03i \end{bmatrix}$	$\begin{bmatrix} 1.00+0.00i & 6.64+4.56i \\ 7.09+4.74i & 0.94-0.08i \end{bmatrix}$
		24	$\begin{bmatrix} 1.00+0.00i & -0.24+0.27i \\ -0.23+0.26i & 0.89+0.03i \end{bmatrix}$	$\begin{bmatrix} 1.00+0.00i & -0.05-0.05i \\ -0.04-0.05i & 0.98+0.01i \end{bmatrix}$	$\begin{bmatrix} 1.00+0.00i & -1.92+0.96i \\ -2.16+1.11i & 1.07-0.06i \end{bmatrix}$	$\begin{bmatrix} 1.00+0.00i & -0.21+1.25i \\ -0.23+1.37i & 0.93-0.04i \end{bmatrix}$
4		20	$\begin{bmatrix} 1.00+0.00i & 0.21+0.60i \\ 0.25+0.64i & 0.87-0.01i \end{bmatrix}$	$\begin{bmatrix} 1.00+0.00i & 0.18-0.10i \\ 0.17-0.10i & 1.03+0.09i \end{bmatrix}$	$\begin{bmatrix} 1.00+0.00i & 0.01+0.33i \\ 0.04+0.33i & 0.94-0.00i \end{bmatrix}$	$\begin{bmatrix} 1.00+0.00i & 0.24-0.34i \\ 0.28-0.32i & 0.99-0.02i \end{bmatrix}$
		22	$\begin{bmatrix} 1.00+0.00i & -0.02+0.02i \\ -0.02+0.02i & 0.96-0.09i \end{bmatrix}$	$\begin{bmatrix} 1.00+0.00i & 0.02-0.08i \\ 0.02-0.07i & 1.06-0.08i \end{bmatrix}$	$\begin{bmatrix} 1.00+0.00i & 0.41-0.25i \\ 0.42-0.25i & 0.94+0.02i \end{bmatrix}$	$\begin{bmatrix} 1.00+0.00i & -0.01-0.08i \\ -0.01-0.07i & 0.98-0.10i \end{bmatrix}$
		24	$\begin{bmatrix} 1.00+0.00i & 0.11+0.63i \\ 0.17+0.58i & 0.95+0.01i \end{bmatrix}$	$\begin{bmatrix} 1.00+0.00i & 0.05-0.13i \\ 0.06-0.13i & 0.98-0.02i \end{bmatrix}$	$\begin{bmatrix} 1.00+0.00i & 0.41+1.14i \\ 0.47+1.26i & 1.02-0.05i \end{bmatrix}$	$\begin{bmatrix} 1.00+0.00i & -0.41+0.49i \\ -0.42+0.54i & 0.97-0.02i \end{bmatrix}$
5		20	$\begin{bmatrix} 1.00+0.0i & -0.18-0.27i \\ -0.17-0.26i & 1.02-0.09i \end{bmatrix}$	$\begin{bmatrix} 1.00+0.00i & 0.08-0.07i \\ 0.08-0.06i & 1.02-0.11i \end{bmatrix}$	$\begin{bmatrix} 1.00+0.00i & -0.04-0.46i \\ -0.08-0.46i & 1.05+0.07i \end{bmatrix}$	$\begin{bmatrix} 1.00+0.00i & 0.26+0.10i \\ 0.24+0.09i & 1.08+0.05i \end{bmatrix}$
		22	$\begin{bmatrix} 1.00+0.00i & 0.60+0.02i \\ 0.55+0.02i & 1.07-0.06i \end{bmatrix}$	$\begin{bmatrix} 1.00+0.00i & 0.03+0.14i \\ 0.03+0.14i & 1.10+0.01i \end{bmatrix}$	$\begin{bmatrix} 1.00+0.00i & -0.17-0.29i \\ -0.15-0.31i & 0.93+0.03i \end{bmatrix}$	$\begin{bmatrix} 1.00+0.00i & -0.42+0.36i \\ -0.45+0.36i & 1.04+0.02i \end{bmatrix}$
		24	$\begin{bmatrix} 1.00+0.00i & 0.16-0.23i \\ 0.16-0.24i & 0.96+0.05i \end{bmatrix}$	$\begin{bmatrix} 1.00+0.00i & -0.12+0.04i \\ -0.10+0.04i & 0.91+0.04i \end{bmatrix}$	$\begin{bmatrix} 1.00+0.00i & 0.18+1.12i \\ 0.17+1.13i & 1.02-0.02i \end{bmatrix}$	$\begin{bmatrix} 1.00+0.00i & 0.71-0.10i \\ 0.73-0.12i & 0.94+0.00i \end{bmatrix}$
6		20	$\begin{bmatrix} 1.00+0.00i & 0.12+0.27i \\ 0.11+0.27i & 1.09+0.00i \end{bmatrix}$	$\begin{bmatrix} 1.00+0.00i & 0.12+0.28i \\ 0.12+0.27i & 1.09+0.01i \end{bmatrix}$	$\begin{bmatrix} 1.00+0.00i & 0.09+0.04i \\ 0.09+0.04i & 0.98+0.04i \end{bmatrix}$	$\begin{bmatrix} 1.00+0.00i & 0.03-0.01i \\ 0.03-0.01i & 0.93+0.01i \end{bmatrix}$
		22	$\begin{bmatrix} 1.00+0.00i & -0.02+0.05i \\ -0.03+0.05i & 1.09-0.02i \end{bmatrix}$	$\begin{bmatrix} 1.00+0.00i & 0.09+0.16i \\ 0.08+0.16i & 1.12+0.03i \end{bmatrix}$	$\begin{bmatrix} 1.00+0.00i & 0.05-0.01i \\ 0.05-0.01i & 0.99-0.01i \end{bmatrix}$	$\begin{bmatrix} 1.00+0.00i & 0.00-0.03i \\ 0.00-0.01i & 1.04-0.03i \end{bmatrix}$
		24	$\begin{bmatrix} 1.00+0.00i & -0.03-0.02i \\ -0.03-0.02i & 1.09-0.01i \end{bmatrix}$	$\begin{bmatrix} 1.00-0.00i & -0.01+0.01i \\ -0.01+0.01i & 0.97-0.10i \end{bmatrix}$	$\begin{bmatrix} 1.00+0.00i & 0.06-0.02i \\ 0.06-0.03i & 0.98+0.08i \end{bmatrix}$	$\begin{bmatrix} 1.00+0.00i & -0.01+0.00i \\ -0.01+0.00i & 0.95+0.03i \end{bmatrix}$

The test results are shown in Table 3. The measurements are performed at different polaristic angles and frequencies. The definition of the four components in the scattering matrix respects the form in (5). Besides, all the components in the scattering matrix are normalized by the value of the S_{pp}. One finds that the complex values of the S_{pp} and S_{qq} in each scattering matrix are similar to each other. Because the chaff elements orientations obey the uniform distribution, which causes unobvious polaristic properties. When examining the cross-polarized components in the scattering matrix, the values of the S_{pq} and S_{qp} components are still close to each

other. This result shows that the chaff cloud generated in this article is unsuitable to be detected using cross-polarization recognition method.

When the polaristic angle of the antenna changes, the magnitudes of the four components within the scattering matrix almost maintain unchanged, but the phase angles of these components are dramatically changing. The possible reason is that the chaff elements are randomly distributed in space, which makes the polarization-matched chaff elements distributed at different distances relative to the antenna within the chaff cloud. This reason also leads to a randomly

(a) Cubic

(b) Corner reflector

(c) Material block.
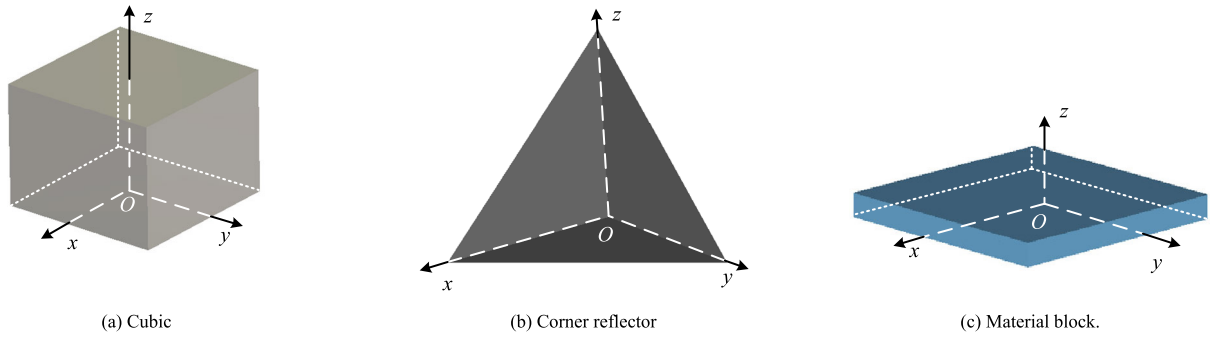
FIGURE 14. Test objects and coordinates system definition.

(a) Case 1, 0°

(b) Case 1, 30°

(c) Case 1, 60°

(d) Case 1, 90°

(e) Case 2, 0°

(f) Case 2, 30°

(g) Case 2, 60°

(h) Case 2, 90°

(i) Case 3, 0°

(j) Case 3, 30°

(k) Case 3, 60°

(l) Case 3, 90°

(m) Case 4, 0°

(n) Case 4, 30°

(o) Case 4, 60°

(p) Case 4, 90°
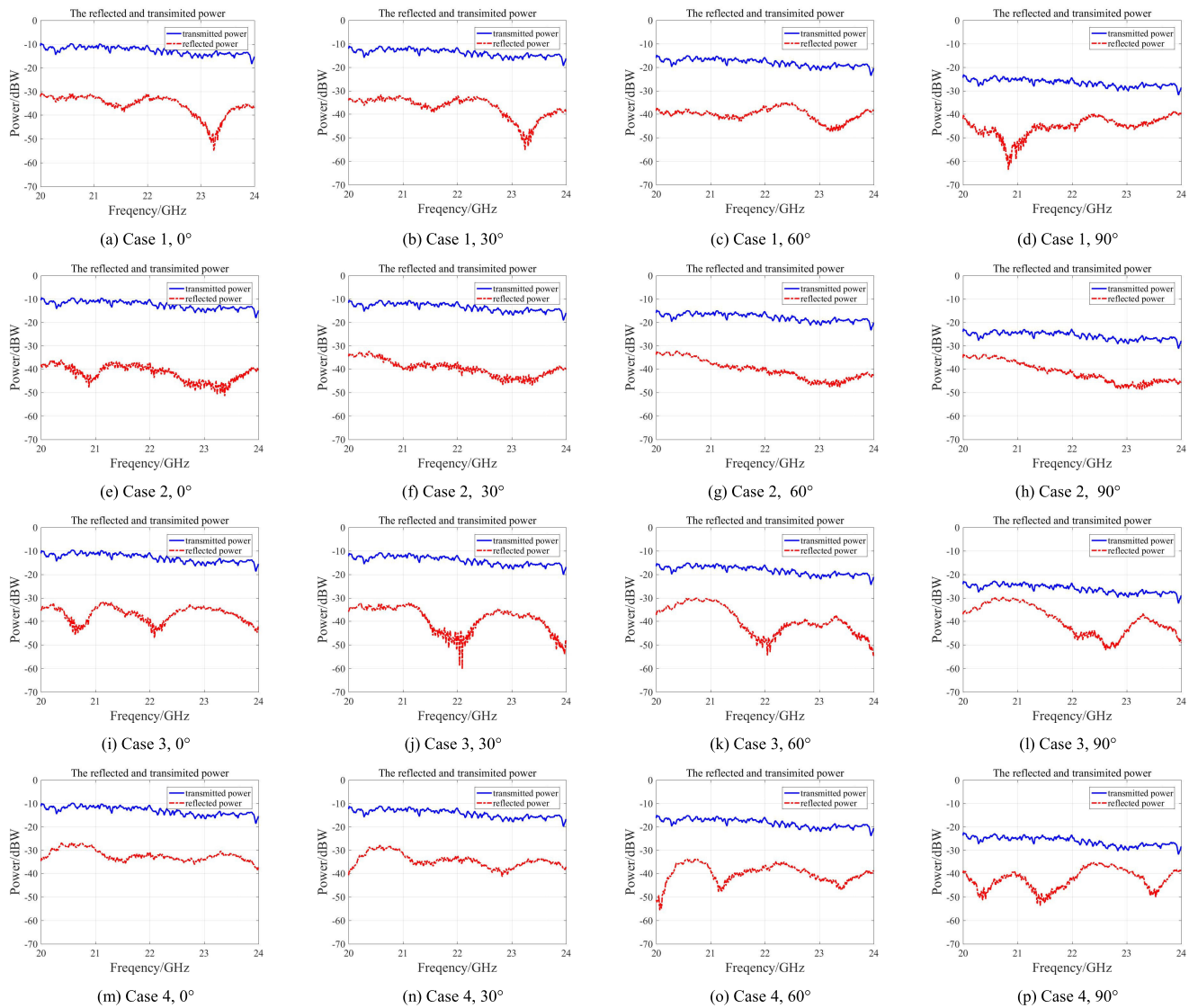
FIGURE 15. The reflected and transmitted power of different types of the chaff cloud.

distributed phase angles of the components in the scattering matrix. These results indicate that it is hard to find the differences between components of the scattering matrix in both amplitude and phase angle for the elements' orientation uniform distributed chaff cloud.

When the test frequency is increasing, there is not a large change occurring for the magnitudes of the co- or cross-polarization components in the scattering matrix. This result indicates that the polaristic scattering properties of the chaff cloud are not sensitive to the frequency changing of the

TABLE 4. Results of the extinction coefficient measurements.

Case 1	0°	10°	20°	30°	40°	50°	60°	70°	80°	90°
20 GHz	140.570	138.572	137.048	134.464	131.877	135.026	132.583	136.000	135.524	137.130
21 GHz	144.783	143.182	141.659	139.643	136.658	139.501	136.371	135.077	138.330	139.471
22 GHz	140.951	139.562	137.860	136.005	132.764	135.818	131.963	135.607	139.421	142.116
23 GHz	148.827	147.530	146.211	144.372	140.208	133.487	141.856	138.034	142.746	143.391
24 GHz	157.882	156.475	155.071	152.887	148.909	142.103	150.947	141.238	144.423	146.568
Case 2	0°	10°	20°	30°	40°	50°	60°	70°	80°	90°
20 GHz	141.549	141.288	139.000	136.498	131.226	134.400	134.132	135.561	138.214	136.527
21 GHz	142.819	142.525	141.176	138.587	132.377	135.852	136.275	138.213	142.809	140.448
22 GHz	145.741	145.429	143.907	141.452	135.320	138.434	135.721	137.613	144.164	141.046
23 GHz	150.402	149.704	148.682	145.678	140.427	133.727	136.208	146.987	145.644	144.880
24 GHz	158.534	157.710	156.549	153.715	148.016	141.602	142.644	148.234	151.079	146.867
Case 3	0°	10°	20°	30°	40°	50°	60°	70°	80°	90°
20 GHz	139.394	138.243	136.585	133.953	128.908	133.221	137.375	139.664	135.162	136.781
21 GHz	140.119	139.586	137.446	134.902	130.289	135.187	139.421	138.962	141.105	139.683
22 GHz	144.953	144.292	142.234	140.042	135.096	139.649	144.602	145.408	136.723	142.663
23 GHz	147.796	147.369	145.220	141.563	137.623	131.926	146.550	147.334	144.734	145.190
24 GHz	155.597	155.230	153.151	149.682	145.699	140.167	156.902	158.403	148.914	151.537
Case 4	0°	10°	20°	30°	40°	50°	60°	70°	80°	90°
20 GHz	138.710	137.519	136.989	133.067	129.385	133.065	136.071	138.746	135.682	138.478
21 GHz	142.943	141.579	141.069	137.503	133.375	136.741	139.757	140.907	137.708	138.633
22 GHz	140.069	138.697	138.193	134.560	130.547	134.030	136.842	138.327	139.863	136.797
23 GHz	148.105	147.147	145.745	142.384	138.323	132.251	146.506	149.378	143.369	144.335
24 GHz	155.078	153.867	152.527	149.209	144.910	138.542	153.317	156.471	151.342	155.342

incident wave. This is mainly because the polaristic scattering characteristics of the chaff corridor are always determined by its geometric shape, material, and the posture in the wave. So, if one wants to change the polarization scattering properties of the chaff cloud, the structure of the chaff elements should be carefully designed to achieve an arbitrary orientation distribution.

When dealing with the shape of the chaff cloud, this article measures different types of the chaff clouds which are described in Table 3. From these test results, one finds that the polarization properties of the chaff cloud are not strongly determined by the shape of the chaff cloud because the chaff elements are separated-defused in the space. This property unlocks the strong dependence of polarization scattering properties on the shape of the chaff cloud. That is to say, the shape of the chaff cloud cannot influence the polarization jamming performance dramatically, which relaxes the diffusion shape requirements. This is one possible reason why the chaff clouds are so widely used.

C. EXTINCTION COEFFICIENT MEASUREMENTS
According to the test principles presented in Section II, the extinction coefficient measurements are performed in the chamber. Test scenario is shown in Fig.13 (d). The chaff

corridor is made as a 5 cm thick board for each case. All of the four models obey the same PDF. The number density of all the chaff boards is 96,000 per 1 m³. The test frequency is from 20 GHz to 24 GHz. The transmitting and receiving devices are selected as the standard Gain horn antennas. The tests are performed at different frequencies and polaristic angles. The transmitted and reflected power of the chaff boards are reported in Table 4 and Fig.15.

From Fig.15, one finds that the reflected power of the chaff board is lower than the transited power. This means that the reflection of the chaff board is very weak as the chaff elements are dispersed distributed in the space and the ratio of the volume of the chaff elements to that of the model is quite small. Therefore, the power of the EM wave can easily pass through the chaff board. This indicates that if one wants to achieve a high reflected power, huge numbers of the chaff elements should be released. From the results in Fig. 15, it also can be seen that the chaff cloud with uniform orientation distribution is not sensitive to changing polaristic angles. When the frequency increases, the values of the reflected and the transmitted power fluctuate as well. But the transmitted power changes relatively small compared with the reflected power. Meanwhile, the transmitted power decreases with the increasing frequency. This result demonstrates that it is harder

for high frequency EM wave to pass through the chaff board. To further prove this point, experiments are conducted at lower frequency $f = 5$ GHz for Case 1 and Case 3 in Table 4. Other simulation conditions are the same to that of Case 1 and Case 3. We measure the extinction coefficient of the chaff corridor under different polaristic angles of 0 degree and 30 degrees. They are 127.338 (Case 1, 0 degree), 126.524 (Case 1, 30 degrees), 115.259 (Case 3, 0 degree), and 112.705. (Case 3, 30 degrees). These results still hold the conclusion that high-frequency wave is hard to pass through the chaff corridor. The possible reason is that the effective electric length of the chaff element is shortened when the wavelength of the incident wave increases, thus resulting in a low reflection power and high transmission properties of the EM wave, vice versa.

Based on these data, the extinction coefficients are calculated and listed in Table 4. At the most polaristic angles, the extinction coefficients are about 140 m^{-1}. These coefficients show that the power of the EM wave to pass through the chaff board drops very quickly. In addition, the values of the extinction coefficients increase with the increasing of the operating frequency. One also finds that the values of the extinction coefficients of the chaff corridor at most polaristic angles are close to each other. This is mainly caused by the random distribution characteristics of the chaff elements. The results also denote that the polaristic extinction coefficients are approximately independent from the polaristic angles. This characteristic provides usage of the chaff cloud to countermeasure the polaristic recognition of the target.

IV. CONCLUSION

This article investigates the scattering matrix and the extinction coefficient measurement methods of the chaff cloud. Initially, the principles of the test are presented. Then, the measurements are performed in a chamber. This article finds that the polaristic scattering properties of the chaff cloud are determined by the orientation distribution of the chaff elements, instead of the shape of the chaff cloud and frequency. Based on the measured data, the extinction coefficients of the chaff cloud are determined. The results show that the extinction coefficients increase with the frequency and are not sensitive to the polaristic angles of the transmitting and receiving antennas. In the future, more models will be made and measured to obtain the statistical polaristic scattering properties of the chaff cloud. In addition, the composite polaristic scattering measurements of the chaff cloud with the target will be conducted in the future.

REFERENCES

[1] W. S. Churchill, *Second World War: Closing the Ring*. New York, NY, USA: Houghton Mifflin, 2010, pp. 201–214.

[2] B. C. F. Butters, "Chaff," *IEE Proc. F Commun., Radar Signal Process.*, vol. 129, no. 3, pp. 197–201, Jun. 1982.

[3] G. Zhu, L. Man, Y. Chen, and H. Yin, "Approach of electromagnetic modeling for chaff clouds formed by exploding," in *Proc. IEEE Int. Conf. Comput. Electromagn. (ICCEM)*, Chengdu, China, Mar. 2018, pp. 1–3.

[4] J. H. Van Vleck, F. Bloch, and M. Hamermesh, "Theory of radar reflection from wires or thin metallic strips," *J. Appl. Phys.*, vol. 18, no. 3, pp. 274–294, Mar. 1947.

[5] A. D. F. Macedo, "Analysis of chaff cloud RCS applying fuzzy calculus," in *IEEE MTT-S Int. Microw. Symp. Dig.*, Natal, Brazil, Aug. 1997, pp. 724–728.

[6] J. S. Lu, G. Zhang, S. Hu, and Y. Yu, "Research on meliorative average RCS of single chaff," in *Proc. World Automat. Congr.*, Puerto Vallarta, Mexico, 2012, pp. 1–4.

[7] P. Peebles, "Bistatic radar cross sections of horizontally oriented chaff," *IEEE Trans. Aerosp. Electron. Syst.*, vol. AES-20, no. 6, pp. 798–809, Nov. 1984.

[8] Y. Guo and H. Uberall, "Bistatic radar scattering by a chaff cloud," *IEEE Trans. Antennas Propag.*, vol. 40, no. 7, pp. 837–841, Jul. 1992.

[9] C. Gang, S. Longfei, M. Jiazhi, and L. Jian, "Identification of chaff interference based on polarization parameter measurement," in *Proc. 13th IEEE Int. Conf. Electron. Meas. Instrum. (ICEMI)*, Yangzhou, China, Oct. 2017, pp. 392–396.

[10] B. Tang, H.-M. Li, and X.-Q. Sheng, "Jamming recognition method based on the full polarisation scattering matrix of chaff clouds," *IET Microw., Antennas Propag.*, vol. 6, no. 13, pp. 1451–1460, Oct. 2012.

[11] P. Pouliguen and L. Desclos, "Model of the polarimetric behavior of chaff media," *Microw. Opt. Technol. Lett.*, vol. 6, no. 3, pp. 214–218, Mar. 1993.

[12] G. Cui, L. Shi, J. Ma, and X. Wang, "Study on chaff diffusion and polarization stratification," in *Proc. IEEE Int. Conf. Comput. Electromagn. (ICCEM)*, Chengdu, China, Mar. 2018, pp. 1–3.

[13] L. Zhang and Z. Wu, "Simulation of full-polarization electromagnetic backscattering characteristics of large number of high-density chaff clouds," in *Proc. Cross Strait Quad-Regional Radio Sci. Wireless Technol. Conf. (CSQRWC)*, Taiyuan, China, Jul. 2019, pp. 1–3.

[14] J. L. Li, Y. Zeng, X. Shen, and L. Wang, "Study on RCS extremum for uniformly oriented chaff cloud," *Radar Sci. Technol.*, vol. 10, no. 3, pp. 316–319, Jun. 2012.

[15] G. Cai, K. Zhang, and Y. H. Li, "Tactical application research of chaff corridor," *Fire Control Command Control*, vol. 33, no. 7, pp. 44–47, Jul. 2008.

[16] H.-W. Wang, H.-X. Wang, and C. Wang, "Beam cutting effect on jamming efficiency of chaff corridor," in *Proc. Asia–Pacific Microw. Conf. (APMC)*, Nanjing, China, Dec. 2015, pp. 1–3.

[17] M. Lv and L. Wang, "Research on the efficiency of the chaff jamming corridor," in *Proc. 4th Int. Conf. Inf. Sci. Control Eng. (ICISCE)*, Changsha, China, Jul. 2017, pp. 1673–1676.

[18] Z. S. Li, Z. Sun, J. Xu, Y. Du, and D. Xu, "Research on model and simulation of chaff centroid jamming for ship," *J. Syst. Simul.*, vol. 21, no. 14, pp. 4203–4206, Jun. 2009.

[19] Z. Yanchun, L. Chunyong, G. Lixin, and L. Songhua, "Evaluation of efficient dielectric constants of chaff corridor in submillimeter band," in *Proc. Int. Conf. Microw. Millim. Wave Technol. (ICMMT)*, Guangzhou, China, May 2019, pp. 1–3.

[20] S. Kownacki, "Screening (Shielding) effect of a chaff cloud," *IEEE Trans. Aerosp. Electron. Syst.*, vol. AES-3, no. 4, pp. 731–734, Jul. 1967.

[21] S. W. Marcus, "Electromagnetic wave propagation through chaff clouds," *IEEE Trans. Antennas Propag.*, vol. 55, no. 7, pp. 2032–2042, Jul. 2007.

[22] F.-M. Shi, W.-D. Xu, C.-Y. Xu, X.-D. Weng, and L. Qin, "The analysis of influence factors of chaff's jamming property in the rainy day," in *Proc. 6th Asia–Pacific Conf. Environ. Electromagn. (CEEM)*, Shanghai, China, Nov. 2012, pp. 88–92.

[23] B. Tang and X. Sheng, "The simulation of statistical characteristics of dense chaff clouds," in *Proc. IEEE Global High Tech Congr. Electron.*, Shenzhen, China, Nov. 2013, pp. 191–194.

[24] A. K. Pandey, "Modeling and simulation of chaff cloud with random orientation and distribution," in *IEEE MTT-S Int. Microw. Symp. Dig.*, New Delhi, India, Dec. 2013, pp. 1–4.

[25] R. Kashyap, V. Kumar, R. K. Gangwar, P. Vasistha, and R. Kumar, "RCS analysis of scaled down chaff clouds using ansys ED(HFSS) to understand the behaviour of real time model," in *IEEE MTT-S Int. Microw. Symp. Dig.*, Kolkata, India, Nov. 2018, pp. 1–4.

[26] L. Chunyong, Z. Yanchun, G. Lixin, and L. Songhua, "Time domain measurement system for chaff cloud scattering evaluation," in *Proc. Int. Conf. Microw. Millim. Wave Technol. (ICMMT)*, Guangzhou, China, May 2019, pp. 1–2.

[27] Y. Chengli, Z. Yanchun, G. Lixin, and L. Songhua, "Measurement scheme of chaff cloud," in *Proc. Int. Conf. Microw. Millim. Wave Technol. (ICMMT)*, Guangzhou, China, May 2019, pp. 1–2.

[28] R. Wang and P. Q. Huang, "RCS measurement of the chaff cloud by instantaneous locking antenna. Method," *Electro-Optic Technol. Appl.*, vol. 2, no. 3, pp. 4–16, Apr. 2001.

[29] Y. H. Zeng, W. Zhang, W. Qin, and J. Meng, "Measurement and analysis on scattering characteristics of chaff cloud," *Electron. Opt. Control*, vol. 17, no. 1, pp. 16–17, Jun. 2010.

[30] L. Zou, X. Wang, and L. Qian, "Development of a chaff cloud RCS measurement radar at 94.5 GHz," *J. Infr., Millim., THz Waves*, vol. 31, no. 11, pp. 1390–1397, Nov. 2010.

[31] Y. Yang, D.-J. Feng, W.-M. Zhang, X.-S. Wang, and S.-P. Xiao, "Detection of chaff centroid jamming aided by GPS/INS," *IET Radar, Sonar Navigat.*, vol. 7, no. 2, pp. 130–142, Feb. 2013.

[32] W. R. Moninger and R. A. Kropfli, "A technique to measure entrainment in cloud by dual-polarization radar and chaff," *J. Atmos. Ocean. Technol.*, vol. 4, no. 1, pp. 75–83, Mar. 1987.

[33] H.-U. Widdel, "Foil chaff clouds as a tool for *in-situ* measurements of atmospheric motions in the middle atmosphere: Their flight behaviour and implications for radar tracking," *J. Atmos. Terr. Phys.*, vol. 52, no. 2, pp. 89–101, Feb. 1990.

[34] A. Ince, I. Vogt, and H. Gossl, "Design of chaff and chaff-supported communication systems," *IEEE Trans. Commun.*, vol. COM-24, no. 8, pp. 785–803, Aug. 1976.

[35] Z. Yanchun, G. Lixin, and X. Donghai, "The near-field scattering of chaff cloud," in *Proc. Cross Strait Quad-Regional Radio Sci. Wireless Technol. Conf. (CSQRWC)*, Xuzhou, China, Jul. 2018, pp. 1–4.

[36] W. Wiesbeck and S. Riegger, "A complete error model for free space polarimetric measurements," *IEEE Trans. Antennas Propag.*, vol. 39, no. 8, pp. 1105–1110, Aug. 1991.

[37] D. E. Shemansky, "CO_2 extinction coefficient 1700–3000 Å," *J. Chem. Phys.*, vol. 56, no. 4, pp. 1582–1587, Feb. 1972.

[38] J. R. Ouimette and R. C. Flagan, "The extinction coefficient of multi-component aerosols," *Atmos. Environ.*, vol. 16, no. 10, pp. 2405–2419, Jan. 1982.

LIXIN GUO (Senior Member, IEEE) received the M.S. degree in radio science from Xidian University, Xi'an, China, in 1993, and the Ph.D. degree in astrometry and celestial mechanics from the Chinese Academy of Sciences, China, in 1999.

From 2001 to 2002, he was a Visiting Scholar with the School of Electrical Engineering and Computer Science, Kyungpook National University, Daegu, South Korea. He has been a Visiting Professor with the d'Energetique des Systemes et Precedes (LESP), University of Rouen, Mont-Saint-Aignan, France, and the Faculty of Engineering and Physical Sciences, University of Manchester, Manchester, U.K. He is currently a Professor and the Head of the School of Physics and Optoelectronic Engineering, Xidian University. He has been the Chief Professor of the Innovative Research Team, Ministry of Science and Technology, China, since 2018. He has authored or coauthored six books and more than 300 journal articles. He has been in charge of and undertaken more than 30 projects. His research interests include electromagnetic wave propagation and scattering in complex and random media, computational electromagnetics, inverse scattering, and antenna analysis and design.

Dr. Guo was a Fellow of the Chinese Institute of Electronics (CIE) and the Vice President of the Physics Institute of Shaanxi Province, China. He was a recipient of the National Science Fund for Distinguished Young Scholars in 2012 and a Distinguished Professor of the Changjiang Scholars Program in 2015.

WEI LIU (Member, IEEE) received the M.S. degree in mechanical engineering and automation and the Ph.D. degree in radio science from Xidian University, Xi'an, China, in 2003 and 2013, respectively.

He is currently an Associate Professor of physics and optoelectronic engineering with Xidian University. His research interests include electromagnetic wave propagation and scattering in complex and random media, and computational electromagnetics.

YANCHUN ZUO received the B.E. degree from Xinyang Normal University, Xinyang, China, in 2013, and the M.E. degree from Xidian University, Xi'an, China, in 2014. He is currently pursuing the D.E. degree in electromagnetic field and microwave technology.

He has published four papers in conference proceedings. His main research interests include electromagnetic scattering modeling and scattering measurements.

JIANYANG DING (Graduate Student Member, IEEE) received the B.E. degree from Xidian University, Xi'an, China, in 2018, where he is currently pursuing the Ph.D. degree in indoor positioning with the School of Telecommunications Engineering. His current research interests include wireless communication and signal processing.

• • •